Investigation of interface deformation dynamics during high–Weber number cylindrical droplet breakup

J.W.J. Kaiser*, J.M. Winter, S. Adami, N.A. Adams

Technical University of Munich, Department of Mechanical Engineering, Chair of Aerodynamics and Fluid Mechanics, Boltzmannstraße 15, 85748 Garching, Germany

ARTICLE INFO

ABSTRACT

In this work, we study the interface deformation during the early-stages of breakup of a water column in an ambient flow field by high-resolution numerical simulation. The compressible Navier–Stokes equations govern the motion of the two fluids, and capillary forces and viscous effects are considered. We model the multiphase flow with a level-set based sharp-interface method with conservative interface interaction. The governing equations are discretized with a finite-volume approach with low-dissipation flux reconstruction at cell faces based on a fifth-order WENO scheme, and a third-order Runge–Kutta TVD explicit time integration scheme. We validate our numerical simulations by comparison with experimental reference data.

We achieve an accurate prediction of wave dynamics and interface deformation of the liquid column. Both flattening of the cylinder (first stage) and shearing of the sheet at the droplet equator (second stage) are reproduced. We show that a distinct pressure-wave pattern forms in the supersonic flow region near the cylinder equator after shock passage. These waves interact with the phase interface, resulting in local interface disturbances that coincide with the onset of the second stage. Resolving these waves is essential for the prediction of the hat-like structure at the upstream face of the cylinder during the second stage of the breakup, which so far only has been observed in experimental visualizations of this particular breakup mode. Our results support the connection of the sheet-stripping mechanism with the local formation of recirculation zones. Extending previous work, our high-resolution results indicate that recirculation zones appear at multiple locations along the interface, and are directly linked to the growth of water sheet-forming interface disturbances.

1. Introduction

The breakup of a spherical liquid drop into smaller fragments is of fundamental importance for many technological applications and environmental phenomena, ranging from internal liquid-fuel combustion engines to manufacturing of medical drugs and splatter of rain drops on supersonic aircrafts (Villermaux, 2007). The initial deformation of the drop is driven by the relative velocity with respect to the ambient flow field, which may be realized by injection into a crossflow or sudden acceleration by shock waves, eventually resulting in drop breakup. The characteristics of the breakup process are determined by the relation of inertial forces, viscous forces, and capillary forces acting on the drop.

The breakup process can be classified by two non-dimensional numbers: the Weber number and the Ohnesorge number, which describe the ratio of inertial to capillary forces and the ratio of viscous to capillary forces, respectively. Different breakup modes have been observed in experimental investigations upon variations of these two parameters, resulting in the postulation of five fundamental breakup regimes: vibrational, bag, multi-mode, sheet-stripping, and catastrophic breakup (Guildenbecher et al., 2009). At small Ohnesorge numbers ($Oh < 0.1$), vibrational and bag modes have been observed for small Weber numbers, and sheet-stripping and catastrophic modes for high Weber numbers. The multi-mode breakup has been assumed to be a transitional mode from bag breakup to sheet-stripping (Dai and Faeth, 2001). It occurs either as bag/plume or plume/sheet-stripping breakup. Theofanous et al.

(2004) suggested a re-classification of the breakup mechanisms, which is motivated by fundamental physical mechanisms that dominate the breakup process: Rayleigh-Taylor piercing (RTP) and shear-induced entrainment (SIE). RTP is the main instability mode for small Weber numbers, and SIE is the terminal instability mode for increasing Weber numbers. The RTP regime is characterized by ambient fluid penetrating the liquid bulk of the drop. The SIE regime, in comparison, exhibits a shearing of liquid material from the "edge" of the drop.

Systematic experimental and numerical investigations of drop breakup for wide parameter ranges have improved the understanding of the breakup process, we refer to reviews by Guildenbecher et al. (2009) and Theofanous (2011). With regard to numerical investigations, Khosla et al. (2006) were among the first to consider a fully three-dimensional setup. They investigated the breakup process in the low Weber number regime. Since then, further three-dimensional studies of the breakup process in the different regimes have been performed, assuming incompressible flow in the RTP regime (Yang et al., 2017) and fully compressible fluid flow in the SIE regime (Meng and Colonius, 2018). Numerical studies often apply (quasi) two-dimensional setups to decrease the required computational cost for breakup simulations. Supporting this simplification, previous experimental studies observed phenomenological similarity of early-stage interface deformation for (quasi) two-dimensional water columns and three-dimensional spherical drops in crossflow in the shear breakup regime (Igra et al., 2002; Igra and Takayama, 2001a), in particular regarding the flattening of the drop / cylinder and shearing at the equator. Experimental results of shock-column interaction (Igra and Takayama, 2001c; 2003; Sembian et al., 2016) often have been used in two-dimensional numerical studies for model validation on shock-interface interaction (Garrick et al., 2017; Igra and Sun, 2010; Ireland and Desjardins, 2016; Nonomura et al., 2014; Schmidmayer et al., 2017; Terashima and Tryggvason, 2009; Wan et al., 2019; Wang et al., 2018; Xiang and Wang, 2017; Yang and Peng, 2019). Also, more detailed physical investigations of the sheet-stripping process have been performed (Aslani and Regele, 2018; Chen, 2008). More specifically, the experimental setup of Igra and Takayama (2001c) has been used in the seminal work of Meng and Colonius for two-dimensional simulations of the breakup of a liquid column in the SIE regime (Meng and Colonius, 2015). Later, they presented fully three-dimensional simulation results of the breakup of a spherical liquid drop at the same flow conditions (Meng and Colonius, 2018). Analyzing both the breakup of the liquid column and the transient flow field, the important role of near-interface recirculation zones in the sheet-stripping process was reported. These zones appeared at the drop equator and in the wake of the drop. Due to the high Weber number and the low Ohnesorge number of the setup, viscous and capillary forces were explicitly suppressed in these simulations.

In the current work, we consider effects of viscous and capillary forces during breakup of a liquid column in the SIE regime. The setup follows that of Igra and Takayama (2001c). We apply a finite volume approach with low-dissipation shock capturing based on WENO reconstruction (Jiang and Shu, 1996) for an accurate representation of small-scale flow structures, and a third-order strongly-stable Runge–Kutta scheme for explicit time integration (Gottlieb and Shu, 1998). A level-set sharp interface method represents the liquid-gas phase interface, and conservative interface-exchange terms determine the interaction of the two phases (Hu et al., 2006; Luo et al., 2015). A block-structured multiresolution scheme with adaptive local timestepping allows for full spatial and temporal adaptivity (Han et al., 2014; Kaiser et al., 2019). The multiresolution compression enables high computational efficiency even at late stages of the interface deformation, as the mesh adapts to the ongoing liquid-column deformation.

Table 1
Material parameters for the stiffened-gas equation-of-state for water and air.

Fluid	γ [-]	p_∞ [GPa]	μ [Pa s]	σ [10^{-3} N/m]
Water	6.12	0.343	1.0×10^{-3}	72.75
Air	1.4	0.0	1.8×10^{-5}	

The structure of the paper is the following: in Section 2, we briefly discuss the physical model. The numerical model is described in Section 3. In Section 4, we study the results of the shock-induced breakup of a liquid column with an initial diameter of $D_0 = 4.8$mm at a shock Mach number of $Ma_S = 1.47$. We compare our results to experimental data of Igra et al. (2002), Igra and Takayama (2001b,c) and Theofanous et al. (2012), and investigate the influence of viscous and capillary effects. We discuss the formation of a hat-like structure on the upstream face of the cylinder which is known from experimental investigations and link it to the interaction of pressure disturbances with the phase interface during the early deformation stages. For quantitative comparison, we introduce the skewness of the axial deformation to quantify small scales during the ongoing deformation and the main breakup stages. We conclude the work in Section 5.

2. Physical model

The governing equations including viscous and capillary forces read in vector notation

$$\frac{\partial \mathbf{U}}{\partial t} + \nabla^T \cdot \mathbf{F} + \nabla^T \cdot \mathbf{F}_\nu = \mathbf{X} \qquad (1)$$

with

$$\mathbf{U} = \begin{pmatrix} \rho \\ \rho\mathbf{u} \\ E \end{pmatrix}, \qquad \mathbf{F} = \begin{pmatrix} \mathbf{u}\rho \\ \rho\mathbf{u} \otimes \mathbf{u} + p\mathbf{I} \\ \mathbf{u}(E+p) \end{pmatrix}, \qquad \text{and} \qquad \mathbf{F}_\nu = \begin{pmatrix} 0 \\ \mathbf{T} \\ \mathbf{T} \cdot \mathbf{u} \end{pmatrix}$$

denoting the vector of conservative states, the convective flux vector, and the viscous flux vector, respectively. Here, ρ denotes the density, t the time, $\mathbf{u}$ the velocity vector, p the pressure, $\mathbf{I}$ the identity matrix, $\mathbf{T}$ the Cauchy stress tensor, and E the total energy

$$E = \rho e + \frac{1}{2}\rho\mathbf{u} \cdot \mathbf{u}, \qquad (2)$$

composed of the internal energy (ρe) and the kinetic energy ($1/2\rho\mathbf{u} \cdot \mathbf{u}$). The vector $\mathbf{X}$ denotes exchange terms between the two phases air and water including capillary and viscous effects, for more details see the following Section 3. The system of equations is closed by the stiffened-gas equation-of-state (EOS)

$$p = (\gamma - 1)\rho e - \gamma p_\infty, \qquad (3)$$

where the ratio of specific heats γ and the background pressure p_∞ are empirically determined parameters. The stiffened-gas EOS has been widely used in simulations with multiple immiscible compressible fluids. We use this EOS for both fluids air and water, for model parameters see Table 1. Note that for the gas phase with $p_\infty = 0$, the stiffened-gas EOS degenerates to the ideal-gas EOS. The parameters for water are calibrated for the given setup following the procedure described in Johnsen and Colonius (2007) with the experimental data of Gojani et al. (2016), see also Meng and Colonius (2015). Note that the stiffened-gas EOS is an incomplete EOS, providing an inaccurate prediction of the temperature. Since we neglect heat transfer, this deficit is not relevant. For a more detailed discussion as well as an extended EOS the reader is referred to Hawker and Ventikos (2012).

As mentioned above, the breakup behavior during aerodynamic fragmentation is dominated by inertial, viscous, and capillary forces. Inertial forces result in a deformation of the drop,
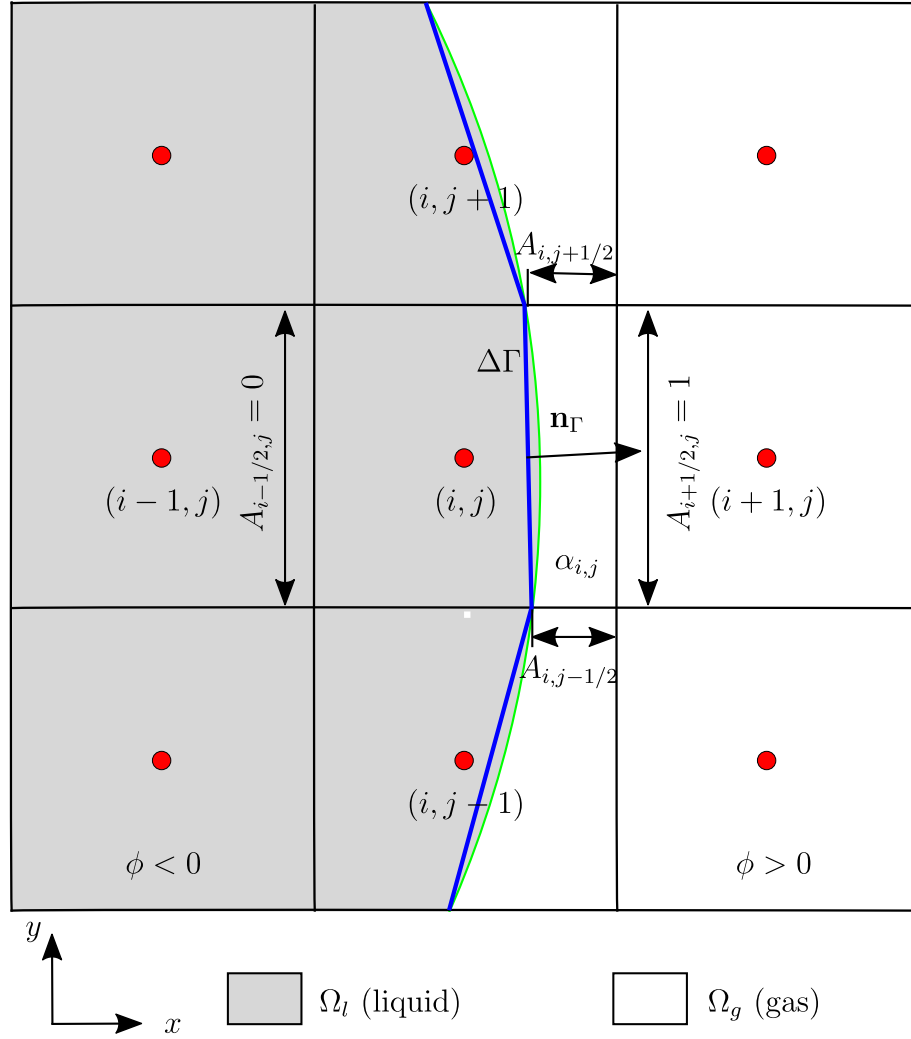
Fig. 1. Schematic finite-volume discretization of the domain Ω on Cartesian square cells. The green line denotes the exact solution, the blue line the linearized approximation by the level-set function. (For interpretation of the references to color in this figure legend, the reader is referred to the web version of this article.)

eventually causing its disintegration, while viscous forces retard the deformation, and capillary forces cause the drop to preserve its spherical shape. Two non-dimensional numbers characterize the breakup process: the Weber number *We* and the Ohnesorge number *Oh*. They describe the ratio of inertial to capillary forces and the ratio of viscous to capillary forces, respectively, and are defined as

$$We = \frac{\rho_{g,s} u_{g,s}^2 D_0}{\sigma} \qquad (4)$$

$$Oh = \frac{\mu_l}{\sqrt{\rho_l d_0 \sigma}} \qquad (5)$$

with the post-shock density of the gas phase $\rho_{g,s}$, the post-shock velocity of the gas phase $u_{g,s}$, the initial droplet diameter D_0, the surface-tension coefficient σ, the dynamic viscosity of the liquid phase μ_l, and the density of the liquid phase ρ_l. Other non-dimensional numbers used to classify secondary atomization are the Reynolds number

$$Re = \frac{\rho_{g,s} u_{g,s} D_0}{\mu_g} \qquad (6)$$

describing the surrounding flow field, the Mach number Ma_S of the shock wave that initiates the breakup process, and the density ratio $\varepsilon = \rho_l / \rho_{g,s}$.

3. Numerical model

3.1. Finite-volume based sharp-interface model with conservative interface interaction

The governing equations (1) are discretized by a finite-volume approach on Cartesian square cells in the domain Ω, which is divided into two subdomains Ω_l (liquid phase) and Ω_g (gaseous phase) by a time-evolving interface Γ. Fig. 1 shows a sketch of the two subdomains with a sharp interface. We integrate Eq. (1) in each computational cell $\Delta_{i,j}$ of each subdomain Ω_m and apply Gauß' theorem to obtain

$$\int_{t^{(n)}}^{t^{(n+1)}} dt \int_{\Delta_{i,j} \cap \Omega_m} d\Delta_{i,j} \frac{\partial \mathbf{U}}{\partial t} + \int_{t^{(n)}}^{t^{(n+1)}} dt \oint_{\partial(\Delta_{i,j} \cap \Omega_m)} (\mathbf{F} + \mathbf{F}_\nu) \cdot \mathbf{n} \, d(\partial \Delta_{i,j})$$

$$= \int_{t^{(n)}}^{t^{(n+1)}} dt \oint_\Gamma \mathbf{X} \cdot \mathbf{n_\Gamma} d\Gamma \qquad (7)$$

where $\Delta_{i,j} = \Delta x_1 \Delta x_2$ denotes the cell volume in two dimensions, $\Delta_{ij} \cap \Omega_m$ each cell volume of phase m, $\partial(\Delta_{ij} \cap \Omega_m)$ the cell face, $\mathbf{n}$ the cell-face normal unit vector, and $\mathbf{n_\Gamma}$ the interface-normal unit vector. We replace $\Delta_{i,j} \cap \Omega_m$ by $\Delta_{i,j}\alpha_{i,j}$, where $\alpha_{i,j}$ is the time-dependent volume fraction of phase m, with $0 \le \alpha_{i,j} \le 1$. The cell

face $\partial(\Delta_{i,j} \cap \Omega_m)$ can be approximated by the cell-face apertures A, $0 \leq A \leq 1$, and the segment of the interface Γ inside this cell, $\Delta\Gamma_{i,j}$. Eq. (7) is then rewritten for a single forward-time integration step of phase m as

$$
\begin{aligned}
\alpha_{i,j}^{(n+1)}\mathbf{U}_{i,j}^{(n+1)} = \; &\alpha_{i,j}^{(n)}\mathbf{U}_{i,j}^{(n)} \\
&+ \frac{\Delta t}{\Delta x_1}\left[A_{i-1/2,j}^{(n)}\left(\mathbf{F}_{i-1/2,j}^{(n)} + \mathbf{F}_{\nu,i-1/2,j}^{(n)}\right) - A_{i+1/2,j}^{(n)}\left(\mathbf{F}_{i+1/2,j}^{(n)} + \mathbf{F}_{\nu,i+1/2,j}^{(n)}\right)\right] \\
&+ \frac{\Delta t}{\Delta x_2}\left[A_{i,j-1/2}^{(n)}\left(\mathbf{F}_{i,j-1/2}^{(n)} + \mathbf{F}_{\nu,i,j-1/2}^{(n)}\right) - A_{i,j+1/2}^{(n)}\left(\mathbf{F}_{i,j+1/2}^{(n)} + \mathbf{F}_{\nu,i,j+1/2}^{(n)}\right)\right] \\
&+ \frac{\Delta t}{\Delta x_1 \Delta x_2}\mathbf{X}_{i,j}^{(n)}(\Delta\Gamma_{i,j})
\end{aligned}
\tag{8}
$$

where Δt denotes the timestep size, $\mathbf{U}_{i,j}$ the cell-averaged state vector of the considered phase in cell (i, j), and $\mathbf{F}_{i,j}$ the fluxes in or out of this cell. The term $\mathbf{X}_{i,j}$ describes momentum and energy exchange between the two fluids in a cell cut by the interface ("cut cell"), and includes inviscid, viscous and capillary effects.

Convective fluxes at cell faces are approximated by the fifth-order WENO (Weighted Essentially Non-Oscillatory) scheme on characteristic fluxes, split by the global Lax-Friedrich (GLF) scheme (Jiang and Shu, 1996; Roe, 1981). Viscous fluxes are discretized with a fourth-order central scheme. For temporal discretization, we use a strongly stable third-order Runge–Kutta scheme (Gottlieb and Shu, 1998; Harten, 1983). The maximum admissible timestep size is determined from a Courant–Friedrichs–Lewy (CFL) stability criterion considering the maximum wave speed, viscous diffusion, and propagation of capillary waves at the interface

$$
\Delta t = \mathrm{CFL} \cdot \min\left(\frac{\Delta x}{\sum|u_i \pm c|_\infty}, \frac{3}{14}\frac{(\Delta x)^2\rho}{\mu}, \sqrt{\frac{\rho_l + \rho_g}{8\pi\sigma}\Delta x^3}\right)
\tag{9}
$$

where c is the speed of sound (Sussman et al., 1994). In all simulations we use CFL$= 0.5$. Advancing the flow field by this timestep size may lead to an unstable fluid state in cells with small volume fraction α. Therefore, we apply a mixing procedure in cells with $\alpha < 0.5$ to maintain numerical stability (Hu et al., 2006).

3.2. Multi-phase treatment

The interaction of the two fluids is solved with the level-set-based conservative interface-interaction model of Hu et al. (2006) with the extension for viscous and capillary forces of Luo et al. (2015). The water-air phase interface is described by a level-set function ϕ. The level-set represents the interface as the zero-crossing of a multi-dimensional continuous function. The liquid subdomain Ω_l is indicated by the negative level-set $\phi(\mathbf{x}) < 0$, the gaseous subdomain Ω_g by the positive level-set $\phi(\mathbf{x}) > 0$, and the interface Γ by the zero-level-set $\phi(\mathbf{x}) = 0$. The absolute value of $\phi(\mathbf{x})$ describes the normal signed distance of the cell center $\mathbf{x}$ to the interface Γ. The level-set is evolved in time with the advection equation

$$
\frac{\partial\phi}{\partial t} + u_\phi\mathbf{n}_\Gamma \cdot \nabla\phi = 0 ,
\tag{10}
$$

with u_ϕ being the level-set advection velocity.

In cut-cells, the level-set advection velocity is equal to the interface velocity u_Γ, which is the contact-wave solution of a two-material Riemann problem at the phase interface, see Luo et al. (2015). The interface velocity u_Γ and the interface pressures $p_{\Gamma,l}$ and $p_{\Gamma,g}$ are obtained from a linearized two-material Riemann solver

$$
u_\Gamma = \frac{\rho_l c_l u_l + \rho_g c_g u_g + p_l - p_g - \sigma\kappa}{\rho_l c_l + \rho_g c_g}
\tag{11}
$$

$$
p_{\Gamma,l} = \frac{\rho_l c_l(p_g + \sigma\kappa) + \rho_g c_g p_l + \rho_l c_l \rho_g c_g(u_l - u_g)}{\rho_l c_l + \rho_g c_g}
\tag{12}
$$

$$
p_{\Gamma,g} = \frac{\rho_l c_l p_g + \rho_g c_g(p_l - \sigma\kappa) + \rho_l c_l \rho_g c_g(u_l - u_g)}{\rho_l c_l + \rho_g c_g} .
\tag{13}
$$

If capillary effects are neglected, i.e. the pressure jump at the interface due to surface tension vanishes, the interface pressures coincide $p_{\Gamma,l} = p_{\Gamma,g} = p_\Gamma$. The curvature κ is the divergence of the interface-normal vector $\kappa = \nabla \cdot \mathbf{n}_\Gamma$, and is numerically obtained from $\mathbf{n}_\Gamma = \nabla\phi/|\nabla\phi|$. The curvature is evaluated at the cell center and then subjected to a subcell correction step to take into account the distance between the cell center and the interface

$$
\kappa_\Gamma = \frac{(D-1)\kappa}{D - 1 - \phi\kappa} ,
\tag{14}
$$

where D is the number of spatial dimensions (Luo et al., 2015). In non-cut cells, the level-set advection velocity is equal to the extrapolated interface velocity $\tilde{u}_\Gamma$, which is determined from the steady-state solution of the extension equation

$$
\frac{\partial\tilde{u}_\Gamma}{\partial\tau} + \mathbf{n}_\Gamma \cdot \nabla\tilde{u}_\Gamma = 0 .
\tag{15}
$$

The numerical solution of the level-set advection does not maintain the signed-distance property $|\nabla\phi| = 1$. Therefore, the re-initialization equation

$$
\frac{\partial\phi}{\partial\tau} + \mathrm{sign}(\phi_0)(|\nabla\phi| - 1) = 0
\tag{16}
$$

is iterated in pseudo time τ to steady state to restore the signed-distance property after each timestep (Sussman et al., 1994). Here, ϕ_0 is the level-set field prior the re-initialization step.

Similarly to the interface velocity extrapolation from cut cells to adjacent bulk cells, the fluid states are extrapolated across the interface to define a "ghost" fluid within the opposing phase (Fedkiw et al., 1999). These ghost-fluid states are used in the reconstruction of the cell-face fluxes near the interface. This approach assures the sharp-interface property of the method.

Momentum and energy exchange across the interface are modeled for phase m by explicit exchange terms

$$
\mathbf{X}_m = \mathbf{X}_{p,m} + \mathbf{X}_\nu
\tag{17}
$$

where

$$
\mathbf{X}_{p,m} = (0, \; p_{\Gamma,m}\Delta\Gamma\mathbf{n}_\Gamma, \; u_\Gamma p_{\Gamma,m}\Delta\Gamma)^T
\tag{18}
$$

represents the inviscid exchange including the pressure jump due to capillarity in liquid ($m = l$) and gas ($m = g$), and

$$
\mathbf{X}_\nu = (0, \; \mathcal{F}_\nu\Delta\Gamma\mathbf{n}_\Gamma, \; (\mathcal{F}_\nu\Delta\Gamma\mathbf{n}_\Gamma) \cdot \mathbf{n}_\Gamma u_\Gamma)^T
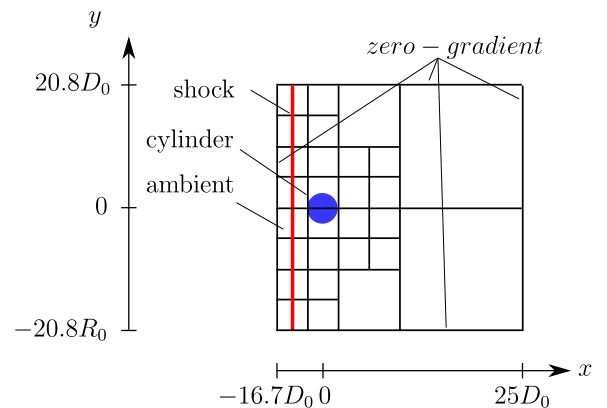\tag{19}
$$

Fig. 2. Sketch of the simulation domain, including an exemplary multiresolution mesh. The water column is sketched in blue, the shock in red. Note that the water column is not drawn to scale. (For interpretation of the references to color in this figure legend, the reader is referred to the web version of this article.)
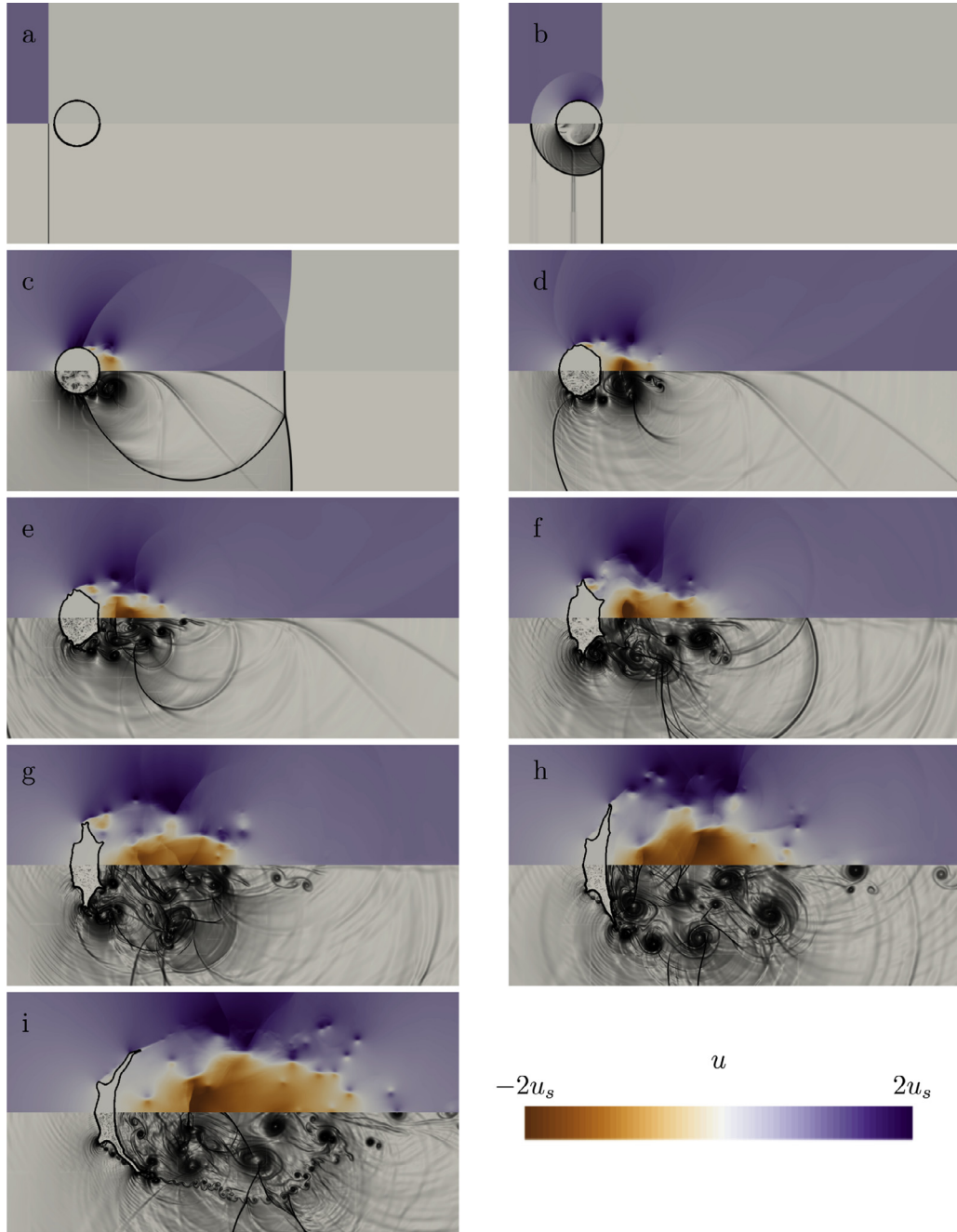
Fig. 3. Normalized streamwise velocity (top) and numerical schlieren images (bottom) of the breakup of a water cylinder with diameter $D_0 = 4.8$mm, initiated by a shock wave with $Ma_S = 1.47$. Shown are different time instants $t^* \in \{0.00, 0.02, 0.11, 0.19, 0.26, 0.44, 0.54, 0.76, 0.98\}$ for the subfigures (a)–(i) (left to right, top to bottom).

models the viscous exchange. Here, $\mathcal{F}_v = [\tau_{xx}, \tau_{xy}; \tau_{yx}, \tau_{yy}]$ is the viscous stress tensor. The length of the interface segment in each cut-cell $\Delta\Gamma_{i,j}$ is computed from the cell-face apertures following

$$\Delta\Gamma_{i,j} = \Delta x \sqrt{\left(A_{i+1/2,j} - A_{i-1/2,j}\right)^2 + \left(A_{i,j+1/2} - A_{i,j-1/2}\right)^2} \qquad (20)$$

(Lauer et al., 2012). Note that more details on the model and in particular generic test cases for model validation can be found in Hu et al. (2006) for the base model and in Luo et al. (2015) for the extended model including capillary and viscous effects.

3.3. Wavelet-based multiresolution approach with adaptive local timestepping

High grid resolution is required to resolve the interface deformation and the surrounding flow field accurately. A coarser resolution is sufficient further away from the cylinder. Therefore, spatial and temporal adaptation techniques are necessary to efficiently solve the breakup process numerically.

We apply a block-structured wavelet-based multiresolution approach based on the work of Harten (1994) to adapt the mesh to the deforming phase interface and the evolving flow field (Han et al., 2014; Hoppe et al., 2019; Rossinelli et al., 2011). The procedure is described in detail in Hoppe et al. (2019). The cell-averaged solution is represented in a hierarchical data structure. Two basic
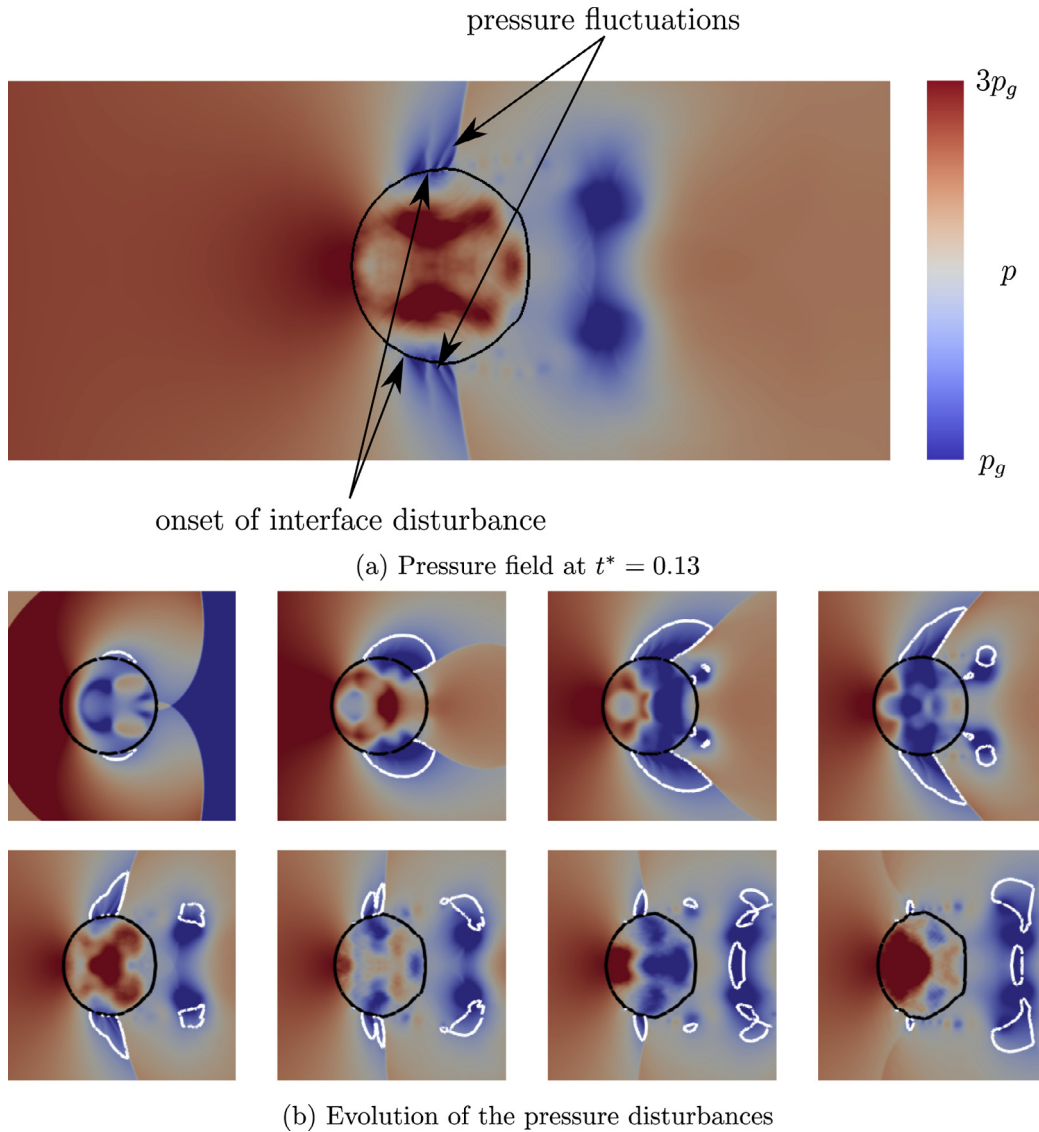
(a) Pressure field at $t^* = 0.13$

(b) Evolution of the pressure disturbances

Fig. 4. (a) Pressure field around the deforming cylinder at $t^* = 0.13$. Pressure fluctuations appear near the equator on the upstream side of the secondary wave system, which is where interface instabilities grow. (b) Temporal evolution of the pressure disturbances. The first frame is at $t^* = 0.033$, subsequent frames follow with $\Delta t^* = 0.022$ from left to right and top to bottom. The white line denotes $Ma = 1$.

operations enable data transfer between successive refinement levels: projection and prediction. The projection operation is applied to obtain data on a refinement level l from the finer level $l + 1$ and corresponds to averaging the cell-states on the finer level. The prediction operation approximates data on level $l + 1$ from level l, and corresponds in our work to a fifth-order interpolation. Projection and prediction are local and consistent, but not commutative: applying first prediction to send data from level l to level $l + 1$ and afterwards projection to send data from level $l + 1$ to level l results in exactly the same solution on level l. To the contrary, applying first projection to send data from level $l + 1$ to level l and afterwards prediction to send data from level l to level $l + 1$ results in an error on level $l + 1$. This motivates the definition of the so called details as the deviation between the exact solution and the predicted solution on any level l. The exact solution on any level l can thus be represented by the exact solution on the coarsest level and the details of all successively finer levels.

Implicit mesh adaption is performed by considering only those details that are larger than a level-dependent threshold

$$\varepsilon_l = \varepsilon_{\text{ref}} \cdot e^{(-D \cdot (l_{max} - l))}, \qquad (21)$$

where l_{max} denotes the maximum level to which the mesh is refined, and ε_{ref} is the admissible relative error on this level. We apply a dyadic refinement strategy, where each cell can be refined into 2^D smaller cells, with a reference error $\varepsilon_{\text{ref}} = 0.01$.

Efficient time integration is obtained by applying a local timestepping approach, where each refinement level is advanced with its level-dependent timestep size (Osher and Sanders, 1983). We use an improved version of this local timestepping scheme which allows for adapting the timestep size after each full Runge–Kutta cycle on the finest refinement level (Kaiser et al., 2019).

4. Results

4.1. Configuration and simulation setup

The numerical domain of the water-cylinder breakup simulation is shown in Fig. 2, together with a schematic multiresolution block structure for this case. Note that we simulate the full cylinder ($D_0 = 4.8$mm), as our previous work indicated asymmetric flow-field patterns in the wake of the cylinder already at early breakup stages (Kaiser et al., 2017). We prescribe zero-gradient boundary
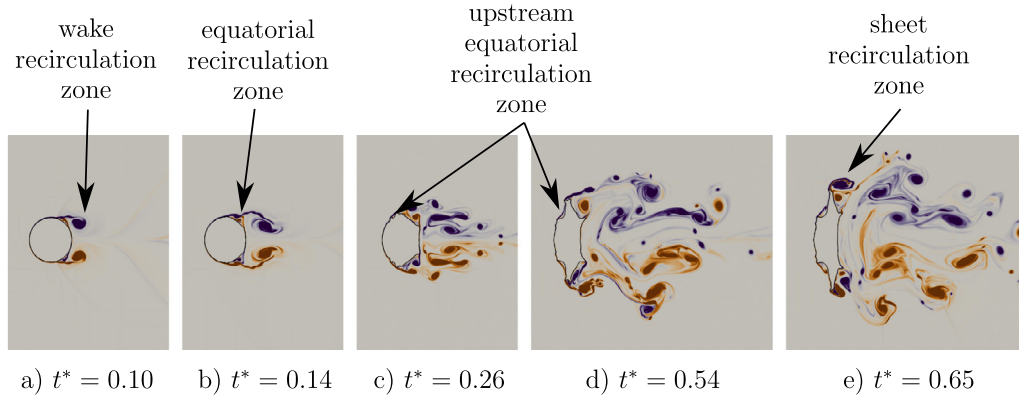
a) $t^* = 0.10$ b) $t^* = 0.14$ c) $t^* = 0.26$ d) $t^* = 0.54$ e) $t^* = 0.65$

Fig. 5. Positive (orange) and negative (purple) z-vorticity streams that interact and form multiple recirculation zones at various instants. (For interpretation of the references to color in this figure legend, the reader is referred to the web version of this article.)
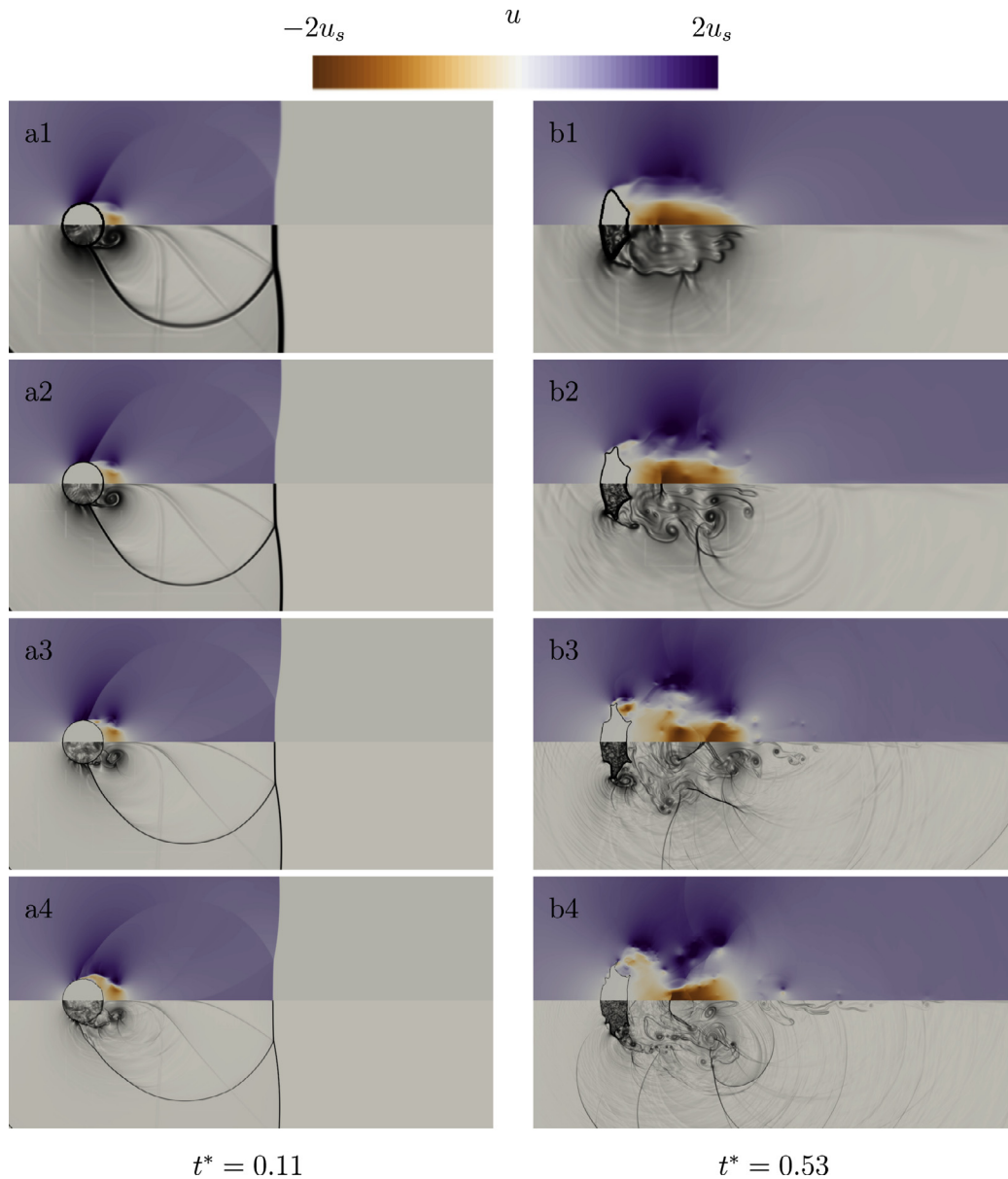

$t^* = 0.11$ $t^* = 0.53$

Fig. 6. The flow field in the vicinity of the water column for resolutions of 50 ((a1) – (b1)), 100 ((a2) – (b2)), 200 ((a3) – (b3)), and 300 ((a4) – (b4)) cells per initial diameter at $t^* = 0.11$ and $t^* = 0.53$. The upper half of each image shows the normalized axial velocity, the lower half numerical schlieren images.
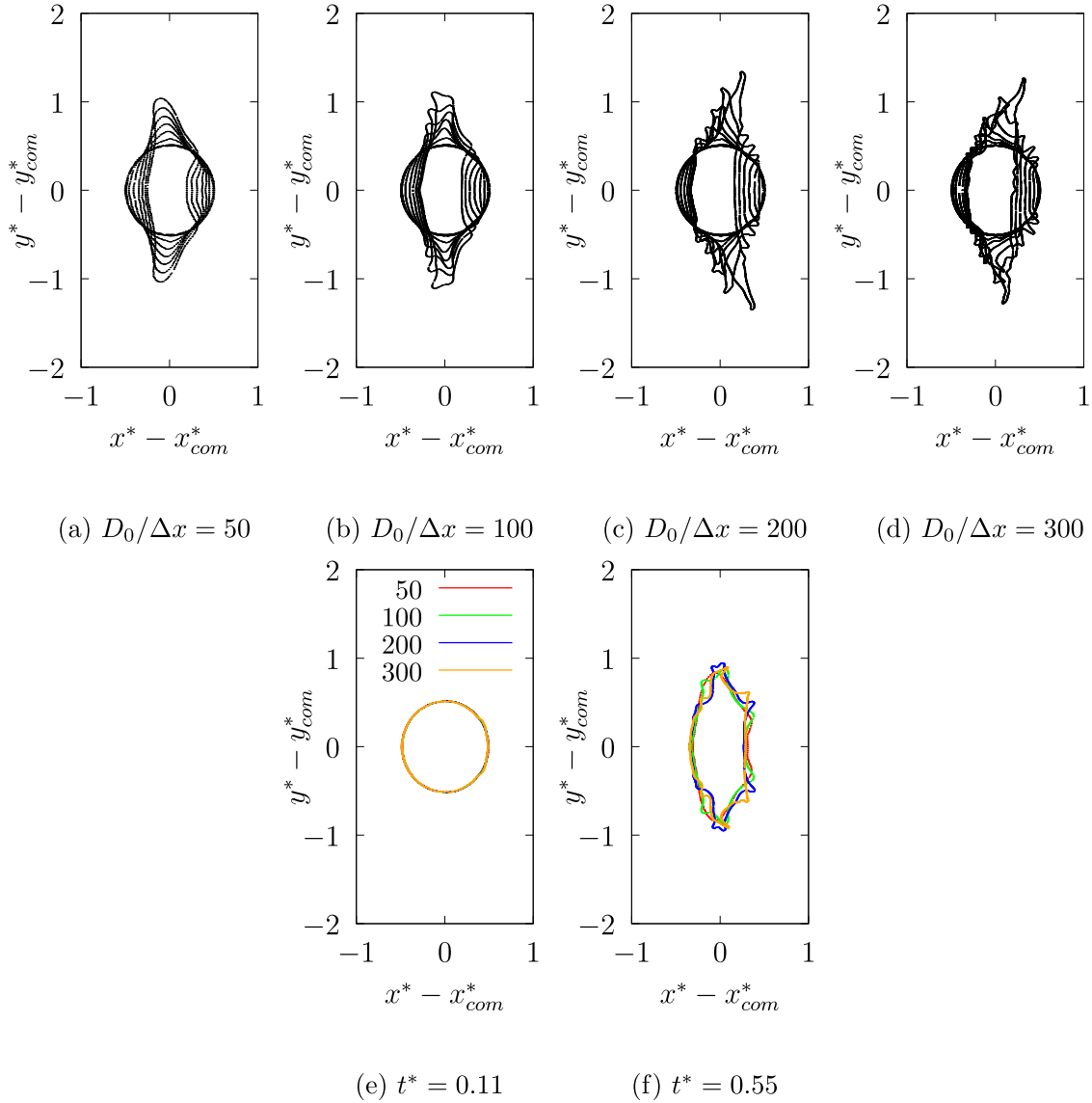
Fig. 7. (a)–(d): Comparison of deformed cylinder interface for resolutions of $D_0/\Delta x = 50$, 100, 200 and 300. The time interval between two subsequent interface contour lines is $\Delta t^* = 0.11$. (e)–(f): the deformed cylinder for these resolutions at $t^* = 0.11$ (e) and $t^* = 0.55$ (f).

conditions at all external boundaries. The domain size is chosen sufficiently large to prevent spurious effects of wave reflections at the domain boundaries.

The ambient uniform flow field is generated by a shock wave. This wave interacts with the cylinder at $t = 0$. Pre-shock air and water are at rest at standard conditions ($\rho_g = 1.20\text{kg/m}^3$, $\rho_l = 1000.0\text{kg/m}^3$, $p_g = p_l = 1.0\text{atm}$). Post-shock conditions follow from the Rankine-Hugoniot relation for a shock Mach number of $Ma_S = 1.47$ ($\rho_{g,s} = 2.18\text{kg/m}^3$, $p_{g,s} = 2.35\text{atm}$, $u_{g,s} = 225.9\text{m/s}$). Material parameters for air and water are given in Table 1. The Weber number of this case is $We = 7.3 \times 10^3$, the Ohnesorge number $Oh = 1.7 \times 10^{-3}$, the Reynolds number $Re = 1.3 \times 10^5$, and the density ratio $\varepsilon = 459$, thus SIE is expected to be the dominating breakup mode. We first perform simulations including viscous and capillary forces with a grid resolution of 200 cells per initial cylinder diameter, which relates to an effective resolution of 8192×8192 cells in the entire domain. Grid-resolution effects are analyzed by varying the resolution from 50 to 300 cells per initial cylinder diameter, which relates to effective resolutions of 2048×2048, 4096×4096, 8192×8192, and 12288×12288 cells. Note that a

full resolution of capillary waves with

$$We_\Delta = \frac{(\rho_l + \rho_{g,s})u_{g,s}^2 \Delta x}{4\pi\sigma} \ll 1 \,, \qquad (22)$$

where We_Δ is the cell Weber number (Popinet, 2018), would imply a resolution of approximately 3×10^5 cells per initial cylinder diameter. Thus, our simulations do not resolve the terminal disintegration of the liquid sheet due to capillary effects. Good agreement with experimental and numerical reference data indicates that the numerical resolution suffices to capture the early stages of the breakup process (see Sections 4.3 and 4.4).

We non-dimensionalize our results using the initial cylinder diameter D_0, the post-shock velocity $u_{g,s}$, the pre-shock pressure p_g, and the characteristic time by Ranger and Nicholls (1969) given by $(D_0\sqrt{\varepsilon})/u_{g,s}$. All non-dimensionalized quantities are denoted by an asterisk (*). Flow direction in all contour plots is from left to right.
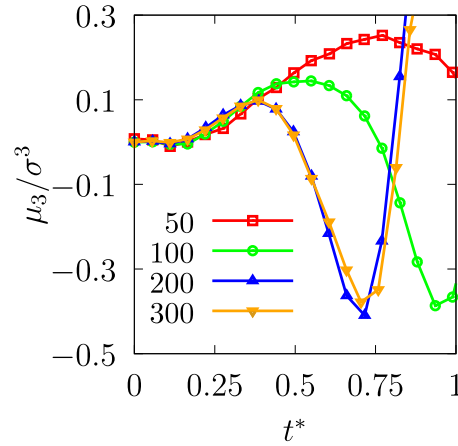
4.2. Overall breakup evolution

Fig. 3 shows the temporal evolution of the numerical breakup simulation results for a resolution of 200 cells per initial diameter,
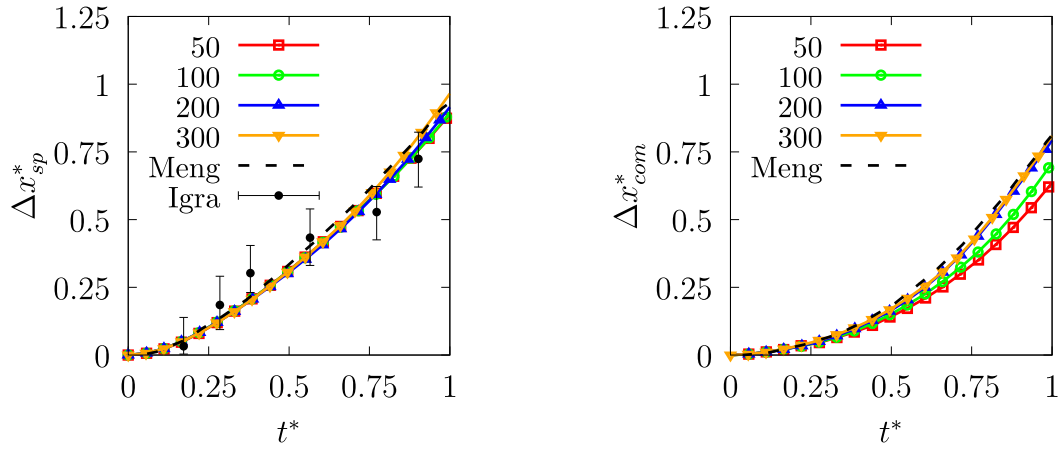
(a) Normalized upstream stagnation point drift

(b) Normalized center-of-mass drift

(c) Skewness

Fig. 8. Evolution of the normalized upstream stagnation point drift (a), the normalized center-of-mass drift (b) and the skewness (c) for various grid resolutions. Where applicable, present results are compared to experimental data of Igra et al. (2002) and Igra and Takayama (2001c) (symbols) and numerical data of Meng and Colonius (2015) (dashed line).

at time instants $t^* \in \{0.00, 0.02, 0.11, 0.19, 0.26, 0.44, 0.54, 0.76, 0.98\}$ (left to right, top to bottom). In each subfigure, the upper half domain displays the streamwise velocity field, and the lower a numerical schlieren image. Following Quirk and Karni (1996), the numerical schlieren images are computed with

$$\phi = e^{-k|\nabla \rho|/\max(|\nabla \rho|)}, \tag{23}$$

where the parameter k is used for scaling the schlieren of different fluids. Here, we use $k = 40$ and $k = 400$ for the air and water phase, respectively (Johnsen and Colonius, 2007; Meng and Colonius, 2015).

The wave patterns in the vicinity of the cylinder agree well with current state-of-the-art simulation results in literature (Meng and Colonius, 2015). Initially, the cylinder is unaffected by the shock passage, as the shock-passage time is much shorter than the relaxation time of the cylinder (Aalburg et al., 2003). The shock wave is partially reflected at the upstream side of the cylinder. Once the angle between the initial shock wave and the water-air interface exceeds a critical value, the reflected shock wave transforms to a Mach reflection (Igra and Takayama, 2001a). The Mach stems merge once the incident shock wave has passed the cylinder and

form a secondary wave system, which eventually travels further upstream along the cylinder's surface (Fig. 3(a)–(c)).

The non-uniform pressure field along the interface results in the flattening of the cylinder (Fig. 3(c)–(e)). At the same time, regular wave-like interface disturbances develop at the equator (Fig. 3(d)). Interface disturbances are related to small pressure fluctuations at the phase interface. These fluctuations are detailed in Fig. 4(a), and their temporal evolution is shown in Fig. 4(b). We observe the formation of a supersonic flow region near the cylinder equator from the location of the sonic line (isoline for $Ma = ||\mathbf{u}||/c = 1$ in white). The pressure fluctuations appear once this supersonic zone reaches the windward side of the cylinder, but do not form on the leeward side. These characteristic waves do not travel upstream with the progressing secondary wave system, but remain at the same location until they merge with the secondary wave system. The pressure waves finally vanish once the secondary wave system detaches from the cylinder interface, and the supersonic flow region disappears. The pressure fluctuations coincide with the onset of the interface waves. We believe that the interaction of these local pressure waves with the phase interface generates small disturbances that trigger interface waves. The in-
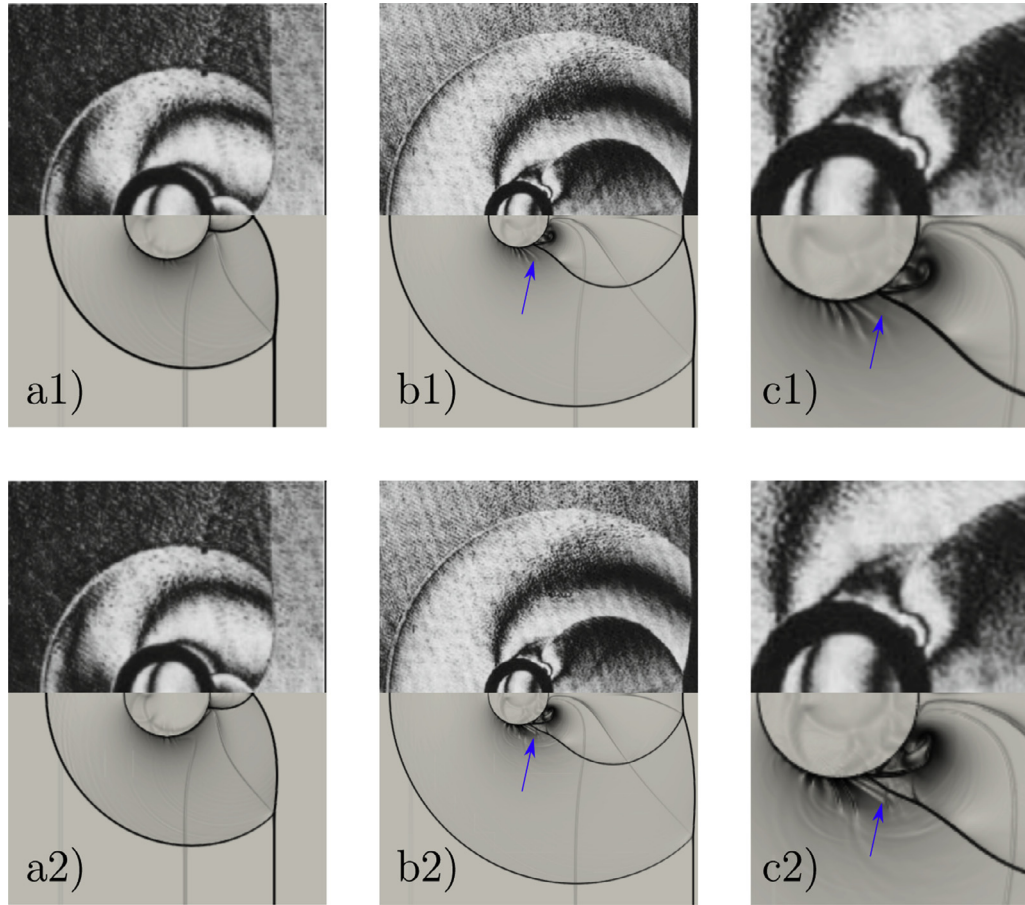
Fig. 9. (a)–(b) Comparison of experimental visualizations of Igra and Takayama (2001b) (upper half) and numerical schlieren images (lower half) at $t^* = 0.035$ ((a); $t = 16.18\mu$s) and $t^* = 0.07$ ((b); $t = 32.14\mu$s). (c) Flow field in the vicinity of the attached secondary wave at $t^* = 0.07$. Shown are results for simulations with resolutions of 200 cells ((a1)–(c1)) and 300 cells ((a2)–(c2)) per initial cylinder diameter. Reprinted from Igra and Takayama (2001b) with permission from Springer.

terface disturbances eventually develop cusps, which merge into a single large water sheet and are stripped off from the cylinder equator (Fig. 3(e)–(h)). The thin sheet is advected further downstream, where it is subjected to strongly fluctuating forces in the unsteady wake of the cylinder and, eventually, breaks up. Our simulations do not resolve this terminal breakup of the sheet. The smallest sheet dimension is limited by the smallest computational cell size.

The simulation confirms the development of a hat-like shape (Fig. 3(f)–(i)) with a smooth windward region and two distinct cusps near the edge, which so far has been reported only in experimental investigations (Theofanous et al., 2012). It is further discussed in the following Section 4.4.

Moreover, multiple recirculation zones establish around the cylinder interface forming during the simulated time until $t^* = 0.98$, whereas Meng and Colonius (2015) have reported a single recirculation zone each in the wake of the cylinder and at the cylinder equator. They play an important role during the deformation and sheet-stripping process, and are initiated by unsteady vortex shedding at the cylinder equator. Fig. 5 shows the z-vorticity at various time instants. Unsteady vortex shedding after the shock passage results in the formation of the wake recirculation zone ($t^* = 0.10$). The shed vortex originating from the cylinder equator is diverted at the downstream stagnation point of the cylinder. It interacts with the vorticity stream near the cylinder equator, which leads to the formation of the equatorial recirculation zone ($t^* = 0.14$). We extend these observations, which agree well with that of Meng and Colonius, by the detection of additional recircu-

lation zones along the interface, which can be related to local unsteady vortex shedding at the deformed interface. Previously mentioned interface disturbances upstream of the cylinder equator are linked to the formation of a recirculation zone on the upstream side of the cylinder near the equator ($t^* = 0.26$), which occurs at later time instants between the hat-like structure on the upstream side and the developing liquid sheet ($t^* = 0.54$). Another recirculation zone forms at the tip of the liquid sheet due to the interaction of multiple vortices in this area, and contributes to the observed flapping of the sheet in the wake of the cylinder ($t^* = 0.65$).

4.3. Grid resolution

We have investigated the effect of the spatial resolution on the numerical results for the cylinder deformation. Fig. 6 depicts contour plots for resolutions of 50 ((a1) – (b1)), 100 ((a2) – (b2)), 200 ((a3) – (b3)), and 300 ((a4) – (b4)) cells per initial cylinder diameter at $t^* = 0.11$ and $t^* = 0.53$. The upper half of each image shows the normalized axial velocity, the lower half shows numerical schlieren.

At $t^* = 0.11$, recirculation zones have formed in the wake of the cylinder and at the equator. Flattening and shift of the upstream stagnation point are similar for all four resolutions. The primary wave system, which consists of the incident and the reflected shock wave, is at the same position for all investigated resolutions. The secondary wave system, which forms near the rear stagnation point once the Mach stems on both sides converge, is attached to the cylinder interface downstream of the equator up
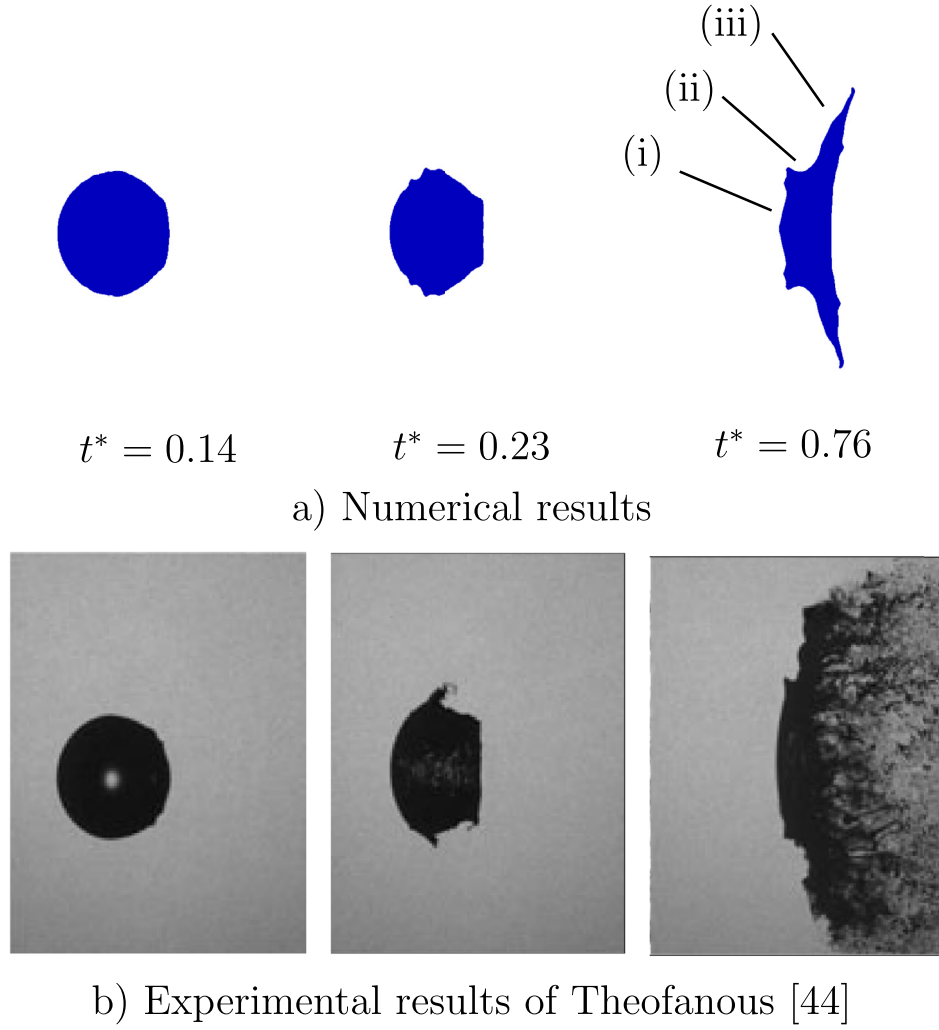
$t^* = 0.14$ $t^* = 0.23$ $t^* = 0.76$

a) Numerical results

b) Experimental results of Theofanous [44]

Fig. 10. Qualitative comparison of the interface deformation process. The experimental figures are obtained from online-available videos. Reprinted from Theofanous et al. (2012), with the permission from AIP Publishing.

to a resolution of 200 cells per diameter. With 300 cells, more details of the local wave-interface interaction are reproduced, and the secondary wave system crosses the cylinder equator slightly earlier (Fig. 6(a4)). This also affects the development of the pressure waves, that are visible in the Schlieren image. They only appear for a resolution of at least 100 cells. For a resolution of 300 cells, the secondary wave system moves further upstream, the supersonic flow region is about to disappear, and pressure waves almost vanish. The resolution of the interface disturbance at the equator requires more than 100 cells per initial diameter (Fig. 6(a1) and (a2)). From grid resolutions of 200 cells per cylinder diameter, interface waves are resolved that are responsible for hat formation and denote the onset of the sheet stripping (Fig. 6(a3) and (a4)).

A similar behavior is found for the results at $t^* = 0.53$. General features such as the recirculation zones are reproduced for all resolutions. Resolutions of at least 200 cells per diameter reproduce the hat-like structure on the upstream side of the cylinder (Fig. 6(b3) and (b4)), while simulations with coarser resolutions exhibit a smooth interface (Fig. 6(b1) and (b2)). Only with sufficient grid resolution, implying sufficiently small numerical dissipation, interface disturbances are accurately resolved and the hat shape develops. This is also the case for the formation of the sheet, which is strongly affected by proper resolution of interface disturbances. With increasing resolution, the sheet exhibits finer details,

see for example the multiple cusps at the edges, each of which is associated with a local recirculation zone (Fig. 6(b2)–(b4)).

Fig. 7 shows the evolution of the phase interface for resolutions of $D_0/\Delta x = 50$, 100, 200 and 300 ((a)–(d)), and overlapping at times $t^* = \{0.11, 0.55\}$ ((e)–(f)). The plots are centered at the respective centers-of-mass

$$\mathbf{x}^*_{com} = \frac{\int_{\Omega_l} \mathbf{x}^* \rho\, dV}{\int_{\Omega_l} \rho\, dV} = \frac{\sum_i \mathbf{x}^*_i \rho_i V_i}{\sum_i \rho_i V_i}, \tag{24}$$

where x^* stands for the cell-center location and Ω_l denotes the liquid subdomain. The time interval between two subsequent grid lines is $\Delta t^* = 0.11$. At the coarsest resolution (Fig. 7(a)), flattening is reproduced, while stripping at the droplet equator is underestimated. The liquid sheet appears for the finer resolution of $D_0/\Delta x = 100$ (Fig. 7(b)). For resolutions of $D_0/\Delta x = 200, 300$, (Fig. 7(c) and (d)) additionally the hat-shaped structure is observed. The overlapping contour lines in subfigures (e) and (f) indicate that coarser grids have a minor effect on typical geometrical parameters. At both instants, the interface overlaps near the upstream and downstream stagnation points, and the extend in streamwise direction is similar. Yet, interface waves are more pronounced for finer resolutions (Fig. 7(e)), and result in a more detailed representation of the sheet and the hat-like structure (Fig. 7(f)).
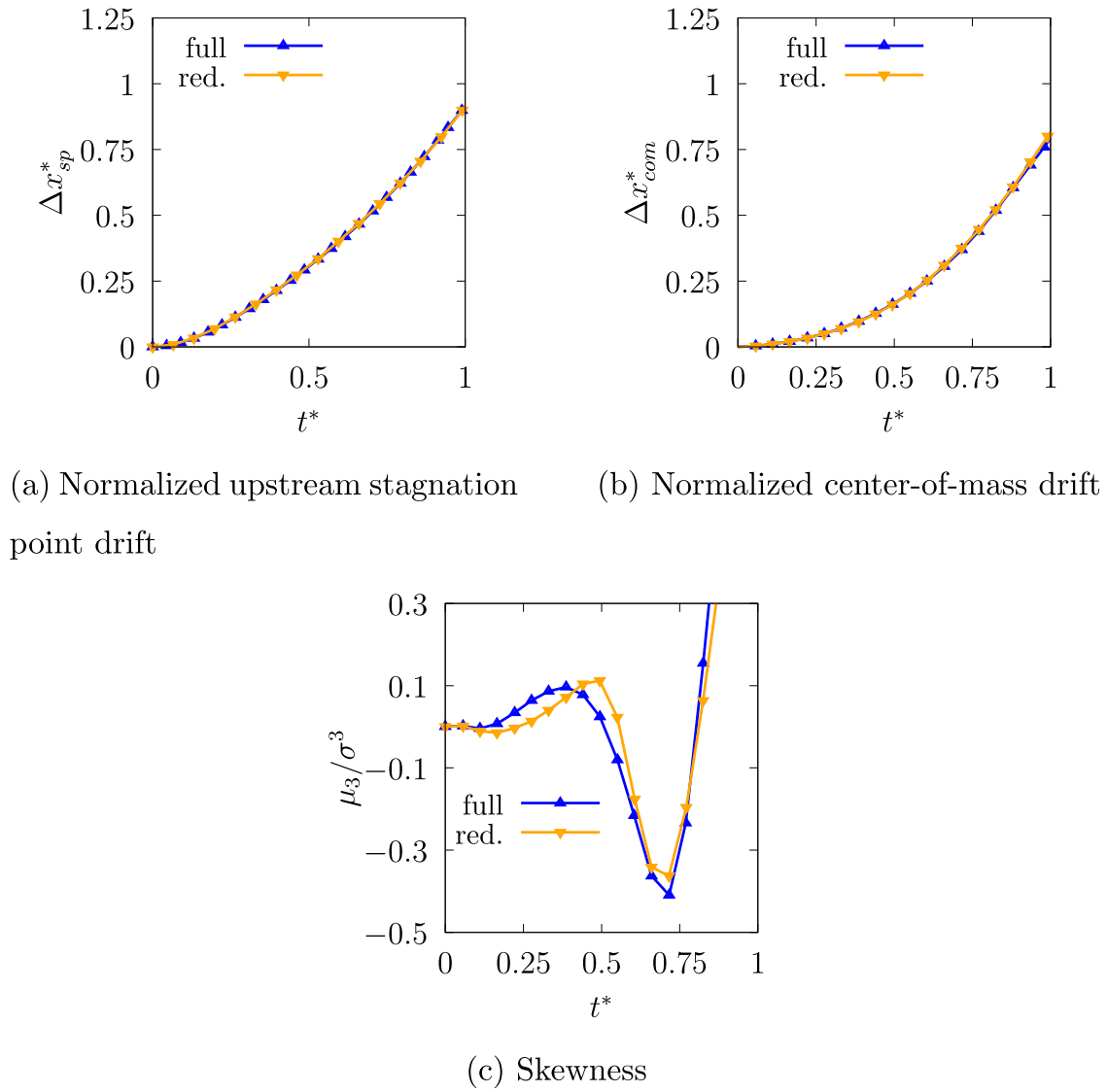
(a) Normalized upstream stagnation
point drift

(b) Normalized center-of-mass drift

(c) Skewness

Fig. 11. Evolution of the normalized upstream stagnation point drift (a), the normalized center-of-mass drift (b) and the skewness (c) for simulations with and without capillary and viscous forces.

A quantitative comparison of the normalized upstream stagnation point drift Δx_{sp}^*, the normalized center-of-mass drift Δx_{com}^*, and the third moment of the axial displacement $\mu_3/\mu_2^{3/2}$ is shown in Fig. 8. Higher-order moments are computed following

$$\mu_k = \int_{\Omega_l} (x^* - x_{com}^*)^k \rho dV = \frac{\sum_i (x_i^* - x_{com}^*)^k \rho_i V_i}{\sum_i \rho_i V_i} . \qquad (25)$$

The second moment ($k = 2$) μ_2 is the variance, and the normalized third moment ($k = 3$) $\mu_3/\mu_2^{3/2}$ the skewness of the mass distribution. The skewness measures the asymmetry between the upstream and the downstream side of the cylinder. For the upstream stagnation point drift, we also show experimental results of Igra et al. (2002) and Igra and Takayama (2001c), and numerical results of Meng and Colonius (2015) for comparison. For the center-of-mass drift, numerical reference data of Meng and Colonius are included. In the study of Meng and Colonius, the authors apply a volume-of-fluid (VOF) approach, and the results are given for a volume faction of $\alpha_T = 0.5$.

The upstream stagnation point drift Δx_{sp}^* (Fig. 8(a)) is converged for the considered resolutions, and agrees well with reference numerical data of Meng and Colonius (2015) and experimen-

tal data of Igra et al. (2002) and Igra and Takayama (2001c). The normalized center-of-mass drift Δx_{com}^* (Fig. 8(b)) is converged for a resolution of 200 cells per initial cylinder radius, and agrees well with the reference solution of Meng and Colonius (2015). This underlines that such integral parameters are insensitive to small scale interface structures which are resolved only for finer meshes. The overall evolution of the cylinder drift is well captured already for fairly coarse resolutions, and remains unaffected by the artificial dissipation of the applied numerical scheme. The skewness plots (Fig. 8(c)) overlap for 200 and 300 cells per initial cylinder diameter, indicating grid convergence. At the higher resolutions, different stages of the drop deformation can be related to the skewness evolution. The initial increase is related to the flattening of the drop. The onset of the hat-like structure at $t^* \approx 0.3$ results in a strong decrease of skewness. From $t^* \approx 0.75$, the liquid sheet is advected downstream, which increases skewness.

In summary, cylinder flattening is least dependent on resolution, and appears already at the coarsest resolution of $D_0/\Delta x = 50$. The most resolution-critical features are interface waves and the formation of the hat shape at the upstream side, which is resolved with $D_0/\Delta x = 200, 300$. Geometrical parameters are less affected by resolution. However, the normalized third moment
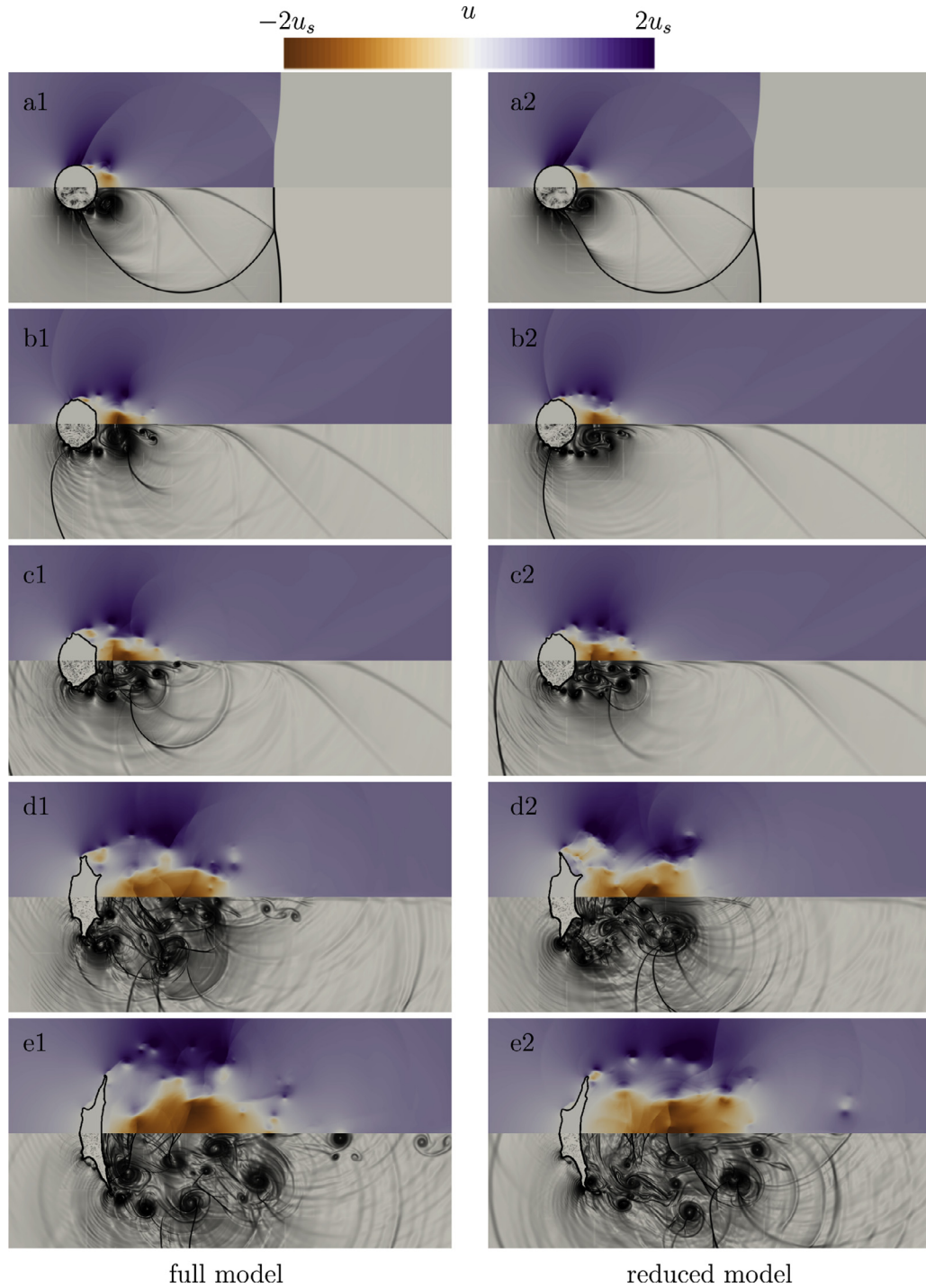
Fig. 12. The flow field in the vicinity of the water column for simulations with capillary and viscous forces ((a1) – (e1)) and without ((a2) – (e2)) for a mesh resolution of 200 cells per initial cylinder diameter at $t^* \in \{0.11, 0.19, 0.26, 0.44, 0.76\}$. The upper half of each image shows the normalized axial velocity field, the lower half numerical schlieren images.

(skewness) appears to deliver a good integral measure to detect the evolution of small-scale features. Our findings extend previously published results (Meng and Colonius, 2015), which showed grid convergence for a resolution of 100 cells per initial diameter. Our results indicate that higher resolutions of at least 200 cells per initial diameter are required, along with low-dissipation temporal and spatial discretization schemes, for resolving detailed breakup features, such as the formation of the upstream hat-shape structure.

4.4. Comparison with experimental visualizations

In the following, we compare our numerical results with available experimental visualizations. Schlieren images reveal wave patterns around the cylinder, as shown in Fig. 9 at times $t^* = 0.035$ (Fig. 9(a); $t = 16.18\mu s$) and $t^* = 0.07$ (Fig. 9(b) and (c); $t = 32.14\mu s$). The experimental images of Igra and Takayama (2001b) are depicted in the upper half, numerical schlieren images in the lower half. Fig. 9(a1)–(c1) give results for a resolution $D_0/\Delta x = 200$, and

Fig. 9(a2)–(c2) for $D_0/\Delta x = 300$. The time instants are chosen as described by Meng and Colonius (2015). At $t = 16.18\mu s$, the numerical simulation accurately reproduces the propagation of the primary wave system (initial and reflected shock), independent of the chosen resolution. The propagation of the secondary wave system, which consists of the converged Mach stems, is slightly underestimated for both resolutions. This delay has been reported previously in literature for this case, e.g. Meng and Colonius (2015). At $t = 32.14\mu s$, the primary waves are accurately predicted by the simulation. The propagation of the wave system close to the interface shows a dependency on the chosen mesh resolutions (see the area marked by the blue arrows in Fig. 9(b), and the focus on this area in Fig. 9(c)). For the higher-resolved simulation ($D_0/\Delta x = 300$), the interaction of the upstream-travelling wave with the increasingly disturbed interface results in a faster progression of the wave in comparison to the simulation with $D_0/\Delta x = 200$, and, thus, in a better agreement with the experimental data.

Igra et al. (2002) and Igra and Takayama (2001a) reported phenomenological similarities for the interface deformation and breakup of two-dimensional liquid columns and three-dimensional spherical drops in the shear breakup regime. With this motivation, we show in Fig. 10 snapshots of the deformed interface from our numerical study of two-dimensional liquid-column breakup (Fig. 10(a)), and qualitatively similar visualizations of three-dimensional drop-breakup experiments of Theofanous et al. (2012) (Fig. 10(b)). The experimental visualizations are taken from a breakup configuration in the SIE regime, with $We = 7.8 \times 10^2$, $Oh = 2.4 \times 10^{-3}$, and $Re = 2.2 \times 10^4$ (run W2 in Theofanous et al. (2012)). We consider the main flow characteristics as precise flow conditions and time information do not match, see also Meng and Colonius (2018) for a corresponding discussion. Nevertheless, the characteristic interface deformation patterns agree well in both visualizations. At $t^* = 0.14$, the cylinder flattens due to the non-uniform pressure distribution along the interface. The downstream side is nearly planar, with two small cusps near the equator. At $t^* = 0.23$, interface waves appear on the upstream side. These disturbances later form the hat-like structure and the liquid sheet, which is typical for this breakup mode ($t^* = 0.76$). The capillary breakup of the sheet in the wake of the cylinder cannot be observed in our simulation, most likely due to resolution limits (see Section 4.1). In summary, the main characteristics of the drop evolution agree with the experiment:

(i) hat-like upstream structure with smooth windward region and two cusps at the edge,
(ii) transition region between hat and sheet, and
(iii) sheet deformation in the wake of the cylinder.

4.5. Capillary and viscous forces

Capillary and viscous forces may be negligible at high Weber and low Ohnesorge numbers. We assess the significance of these forces on overall breakup evolution and on interface deformation for the given set of physical and numerical parameters. Fig. 11 shows the temporal evolution of the upstream stagnation point drift, the center-of-mass drift, and the skewness of the deformation in x-direction for simulations with and without capillary and viscous effects for a resolution of 200 cells per initial diameter. The upstream stagnation point drift Δx_{sp}^* (Fig. 11(a)) and the center-of-mass drift Δx_{com}^* (Fig. 11(b)) overlap, indicating that capillary and viscous effects are insignificant at the considered We and Oh. Generally, also the skewness (Fig. 11(c)) shows similar evolution through the main stages: increase during the flattening stage,

decrease during the hat-formation, and subsequent increase during sheet stripping. However, for $t^* < 0.5$, the skewness differs more significantly, indicating that small scale interface structures at early deformation stages indeed are affected by surface tension and viscous forces. With progressing interface deformation, inertial forces dominate and overwhelm capillary and viscous effects.

Fig. 12 shows contour plots at time instants $t^* \in \{0.11, 0.19, 0.26, 0.44, 0.76\}$ (top to bottom) for the cases with ((a1) – (e1)) and without ((a2) – (e2)) capillary and viscous forces. The upper half domain shows the normalized axial velocity, the lower numerical schlieren images. The general flow-field and interface-deformation evolution agree well qualitatively for both cases. However, the formation of the two small water sheets on the leeward side of the cylinder is delayed ($t^* = 0.19, 0.26$) when neglecting capillary and viscous effects. Also, interface disturbances at the equator appear to be sharper ($t^* = 0.19, 0.26$), which has some effect on the shape of the sheet at later instants ($t^* = 0.76$). Nonetheless, flow field characteristics such as the recirculation zones are well reproduced in both cases. At $t^* = 0.76$, both cases exhibit the hat-shape structure at the upstream side and the liquid sheet at the downstream side.

5. Conclusion

We have analyzed interface deformation of shock-induced breakup of a liquid column by simulation with a high-resolution numerical scheme. The numerical model has beed validated by comparison with experimental results of Igra et al. (2002), Igra and Takayama (2001b,c) and Theofanous et al. (2012). The analysis focuses on the unsteady deformation of the water cylinder for different mesh resolutions, and on comparison of results for simulations with and without capillary and viscous forces.

The simulations accurately predict wave dynamics and interface deformation of the liquid column, reproducing the flattening of the cylinder (first stage) and the stripping of the sheet (second stage). Pressure waves form in a supersonic region upstream of the cylinder equator after shock impact and interact with the phase interface. This results in local interface disturbances, coinciding with the onset of the second stage. Resolving these interface waves is essential for a numerical prediction of a hat-shape structure at the upstream side of the cylinder during the second stage of the breakup, which is found in experimental results of Theofanous et al. (2012) for this breakup mode. To our knowledge, this structure has not been reproduced by numerical simulations in previous works. We assume that the pressure waves initiate the interface disturbances, since these pressure waves also appear for a coarser resolution of 100 cells per initial diameter, for which the interface remains smooth due to numerical dissipation. The results confirm the relation between the sheet-stripping mechanisms and the local formation of recirculation zones, as reported by Meng and Colonius (2015). Extending their findings, we find that additional recirculation zones appear at multiple locations near the interface, and are directly linked to the evolution of liquid sheets from interface disturbances. At very early stages of the shock-column interaction, correct prediction of the interaction between the secondary wave system and interface instabilities is critical for qualitative agreement between simulation and experimental results of Igra and Takayama (2001b). A comparative study shows that capillary and viscous forces have small effect on integral parameters for the considered Weber and Ohnesorge numbers and for the early stages of breakup. Late stages of breakup evolution increasingly develop three-dimensional flow structures. Simulations and analyses of three-dimensional configurations at late breakup stages are subject of ongoing work.

Declaration of Competing Interest

The authors declare that they have no known competing financial interests or personal relationships that could have appeared to influence the work reported in this paper.

CRediT authorship contribution statement

J.W.J. Kaiser: Conceptualization, Methodology, Software, Investigation, Formal analysis, Visualization, Writing - original draft. **J.M. Winter:** Methodology, Software, Investigation, Writing - original draft, Writing - review & editing. **S. Adami:** Writing - review & editing, Supervision, Resources, Project administration. **N.A. Adams:** Formal analysis, Writing - review & editing, Supervision, Funding acquisition, Project administration.

Acknowledgments

References

Aalburg, C., van Leer, B., Faeth, G.M., 2003. Deformation and drag properties of round drops subjected to shock-wave disturbances. AIAA J. 41 (12), 2371–2378.

Aslani, M., Regele, J.D., 2018. A localized artificial diffusivity method to simulate compressible multiphase flows using the stiffened gas equation of state. Int. J. Numer. Methods Fluids 88 (9), 413–433. doi:10.1002/fld.4668.

Chen, H., 2008. Two-dimensional simulation of stripping breakup of a water droplet. AIAA J. 46 (5), 1135–1143.

Dai, Z., Faeth, G.M., 2001. Temporal properties of secondary drop breakup in the multimode breakup regime. Int. J. Multiphase Flow 27, 217–236.

Fedkiw, R.P., Aslam, T.D., Merriman, B., Osher, S., 1999. A non-oscillatory Eulerian approach to interfaces in multimaterial flows (the ghost fluid method). J. Comput. Phys. 152 (2), 457–492.

Garrick, D.P., Owkes, M., Regele, J.D., 2017. A finite-volume HLLC-based scheme for compressible interfacial flows with surface tension. J. Comput. Phys. 339, 46–67. doi:10.1016/j.jcp.2017.03.007.

Gojani, A.B., Ohtani, K., Takayama, K., Hosseini, S.H., 2016. Shock Hugoniot and equations of states of water, castor oil, and aqueous solutions of sodium chloride, sucrose and gelatin. Shock Waves 26, 63–68.

Gottlieb, S., Shu, C.-W., 1998. Total variation diminishing Runge–Kutta schemes. Math. Comput. 67 (221), 73–85.

Guildenbecher, D.R., López-Rivera, C., Sojka, P.E., 2009. Secondary atomization. Exp. Fluids 46 (3), 371–402. doi:10.1007/s00348-008-0593-2.

Han, L.H., Hu, X.Y., Adams, N.A., 2014. Adaptive multi-resolution method for compressible multi-phase flows with sharp interface model and pyramid data structure. J. Comput. Phys. 262, 131–152. doi:10.1016/j.jcp.2013.12.061.

Harten, A., 1983. High resolution schemes for hyperbolic conservation laws. J. Comput. Phys. 135, 260–278. doi:10.1016/0021-9991(83)90136-5.

Harten, A., 1994. Adaptive multiresolution Schemes for Shock Computations. J. Comput. Phys. 115, 319–338.

Hawker, N.A., Ventikos, Y., 2012. Interaction of a strong shockwave with a gas bubble in a liquid medium: a numerical study. J. Fluid Mech. 701, 59–97. doi:10.1017/jfm.2012.132.

Hoppe, N., Pasichnyk, I., Allalen, M., Adami, S., Adams, N.A., 2019. Node-level optimization of a 3D block-based multiresolution compressible flow solver with emphasis on performance portability. In: Proceedings of the International Conference on High Performance Computing & Simulation (HPCS).

Hu, X., Khoo, B., Adams, N., Huang, F., 2006. A conservative interface method for compressible flows. J. Comput. Phys. 219 (2), 553–578. doi:10.1016/j.jcp.2006.04.001.

Igra, D., Ogawa, T., Takayama, K., 2002. A parametric study of water column deformation resulting from shock wave loading. At. Sprays 12, 577–591. doi:10.1615/AtomizSpr.v12.i56.20.

Igra, D., Sun, M., 2010. Shock–water column interaction, from initial impact to fragmentation onset. AIAA J. 48, 2763–2771.

Igra, D., Takayama, K., 2001. Investigation of aerodynamic breakup of a cylindrical water droplet. At. Sprays 11, 167–185.

Igra, D., Takayama, K., 2001. Numerical simulation of shock wave interaction with a water column. Shock Waves 11 (3), 219–228.

Igra, D., Takayama, K., 2001. A study of shock wave loading on a cylindrical water column. Technical Report. Institute of Fluid Science, Tohoku University.

Igra, D., Takayama, K., 2003. Experimental investigation of two cylindrical water columns subjected to planar shock wave loading. J. Fluids Eng. 125 (2), 325–331. doi:10.1115/1.1538628.

Ireland, P.J., Desjardins, O., 2016. Toward liquid jet atomization in supersonic crossflows. In: Proceedings of the ILASS AmericasTwenty-eighth Annual Conference on Liquid Atomization and Spray Systems.

Jiang, G.-S., Shu, C.-W., 1996. Efficient implementation of weighted ENO schemes. J. Comput. Phys. 126, 202–228.

Johnsen, E., Colonius, T., 2007. Numerical simulations of non-spherical bubble collapse with applications to shockwave lithotripsy. California Institute of Technology, Pasadena, CA.

Kaiser, J.W.J., Adami, S., Adams, N.A., 2017. Direct numerical simulation of shock-induced drop breakup with a sharp-interface-method. In: Proceedings of the Tenth International Symposium on Turbulence and Shear Flow Phenomena, TSFP 2017, pp. 1–6.

Kaiser, J.W.J., Hoppe, N., Adami, S., Adams, N.A., 2019. An adaptive local time-stepping scheme for multiresolution simulations of hyperbolic conservation laws. J. Comput. Phys. X 4, 1000038.

Khosla, S., Smith, C.E., Throckmorton, R.P., 2006. Detailed understanding of drop atomization by gas crossflow using the volume of fluid method. In: Proceedings of the Nineteenth Annual Conference on Liquid Atomization and Spray Systems (ILASS-Americas), Toronto, Canada.

Lauer, E., Hu, X.Y., Hickel, S., Adams, N.A., 2012. Numerical investigation of collapsing cavity arrays. Phys. Fluids 24 (5), 052104. doi:10.1063/1.4719142.

Luo, J., Hu, X., Adams, N., 2015. A conservative sharp interface method for incompressible multiphase flows. J. Comput. Phys. 284, 547–565. doi:10.1016/j.jcp.2014.12.044.

Meng, J.C., Colonius, T., 2015. Numerical simulations of the early stages of high-speed droplet breakup. Shock Waves 25, 339–414.

Meng, J.C., Colonius, T., 2018. Numerical simulation of the aerobreakup of a water droplet. J. Fluid Mech. 835, 1108–1135. doi:10.1017/jfm.2017.804.

Nonomura, T., Kitamura, K., Fujii, K., 2014. A simple interface sharpening technique with a hyperbolic tangent function applied to compressible two-fluid modeling. J. Comput. Phys. 258, 95–117. doi:10.1016/j.jcp.2013.10.021.

Osher, S., Sanders, R., 1983. Numerical approximations to nonlinear conservation laws with locally varying time and space grids. Math. Comput. 41 (164), 321–336.

Popinet, S., 2018. Numerical models of surface tension. Annu. Rev. Fluid Mech. 50 (1), 49–75. doi:10.1146/annurev-fluid-122316-045034.

Quirk, J.J., Karni, S., 1996. On the dynamics of a shock-bubble interaction. J. Fluid Mech. 318, 129–163.

Ranger, A.A., Nicholls, J.A., 1969. Aerodynamic shattering of liquid drops.. AIAA J. 7 (2), 285–290. doi:10.2514/3.5087.

Roe, P.L., 1981. Approximate Riemann solvers, parameter vectors, and difference schemes. J. Comput. Phys. 43 (2), 357–372.

Rossinelli, D., Hejazialhosseini, B., Spampinato, D.G., Koumoutsakos, P., 2011. Multicore/multi-gpu accelerated simulations of multiphase compressible flows using wavelet adapted grids. J. Sci. Comput. 33 (2), 512–540.

Schmidmayer, K., Petitpas, F., Daniel, E., Favrie, N., Gavrilyuk, S., 2017. A model and numerical method for compressible flows with capillary effects. J. Comput. Phys. 334, 468–496.

Sembian, S., Liverts, M., Tillmark, N., Apazidis, N., 2016. Plane shock wave interaction with a cylindrical water column. Phys. Fluids 28 (5). doi:10.1063/1.4948274.

Sussman, M., Smereka, P., Osher, S., 1994. A level set approach for computing solutions to incompressible two-phase flow. J. Comput. Phys. 114, 146–159.

Terashima, H., Tryggvason, G., 2009. A front-tracking/ghost-fluid method for fluid interfaces in compressible flows. J. Comput. Phys. 228 (11), 4012–4037. doi:10.1016/j.jcp.2009.02.023.

Theofanous, T., 2011. Aerobreakup of Newtonian and viscoelastic liquids. Annu. Rev. Fluid Mech. 43 (1), 661–690. doi:10.1146/annurev-fluid-122109-160638.

Theofanous, T., Mitkin, V.V., Ng, C.L., Chang, C.H., Deng, X., Sushchikh, S., 2012. The physics of aerobreakup. Part II. Viscous liquids. Phys. Fluids 24.

Theofanous, T.G., Li, G.J., Dinh, T.N., 2004. Aerobreakup in rarefied supersonic gas flows. J. Fluids Eng. 126 (4), 516. doi:10.1115/1.1777234.

Villermaux, E., 2007. Fragmentation. Annu. Rev. Fluid Mech. 39, 419–446. doi:10.1016/j.physa.2006.04.087.

Wan, Q., Deiterding, R., Eliasson, V., 2019. Numerical investigation of shock wave attenuation in channels using water obstacles. Multisc. Multidiscip. Model. Exp. Des. 2, 159–173.

Wang, B., Xiang, G., Hu, X.Y., 2018. An incremental-stencil WENO reconstruction for simulation of compressible two-phase flows. Int. J. Multiphase Flow 104, 20–31.

Xiang, G., Wang, B., 2017. Numerical study of a planar shock interacting with a cylindrical water column embedded with an air cavity. J. Fluid Mech. 825, 825–852. doi:10.1017/jfm.2017.403.

Yang, H., Peng, J., 2019. Numerical study of the shear-thinning effect on the interaction between a normal shock wave and a cylindrical liquid column. Phys. Fluids 31 (4). doi:10.1063/1.5083633.

Yang, W., Jia, M., Che, Z., Sun, K., Wang, T., 2017. Transitions of deformation to bag breakup and bag to bag-stamen breakup for droplets subjected to a continuous gas flow. Inter. J. Heat Mass Transf. 111, 884–894. doi:10.1016/j.ijheatmasstransfer.2017.04.012.